Effect of hot cracking on the mechanical properties of Hastelloy X superalloy fabricated by laser powder bed fusion additive manufacturing

Quanquan Han[a,b*], Yuchen Gu[c], Shwe Soe[b], Franck Lacan[b], Rossitza Setchi[b*]

[a]Centre for Advanced Jet Engineering Technologies (CaJET), Key Laboratory of High Efficiency and Clean Mechanical Manufacture, Centre for Additive Manufacturing, School of Mechanical Engineering, Shandong University, Jinan 250061, China

[b]Cardiff School of Engineering, Cardiff University, Cardiff CF24 3AA, UK

[c]College of Engineering, Swansea University, Swansea, SA1 8EN, UK

Corresponding authors: Quanquan Han: Hanq1@cardiff.ac.uk, +4402920876266

Rossitza Setchi: Setchi@cardiff.ac.uk, +4402920875720

Abstract

Nickel-based superalloys such as Hastelloy X (HX) are widely used in gas turbine engine applications and the aerospace industry. HX is susceptible to hot cracking, however, when processed using additive manufacturing technologies such as laser powder bed fusion (LPBF). This paper studies the effects of minor alloying elements on microcrack formation and the influences of hot cracking on the mechanical performance of LPBF-fabricated HX components, with an emphasis on the failure mechanism of the lattice structures. The experimental results demonstrate that a reduction in the amount of minor alloying elements used in the alloy results in the elimination of hot cracking in the LPBF-fabricated HX; however, this modification degrades the tensile strength by around 140 MPa. The microcracks were found to have formed uniformly at the high-angle grain boundaries, indicating that the cracks were intergranular, which is associated with Mo-rich carbide segregation. The study also shows that the plastic-collapse strength tends to increase with increasing strut sizes (i.e. relative density) in both the 'with cracking' and 'cracking-free' HX lattice structures, but the cracking-free HX exhibit a higher strength value. Under compression, the cracking-free HX lattice structures' failure mechanism is controlled by plastic yielding, while the failure of the with-cracking HX is dominated by plastic buckling due to the microcracks formed within the LPBF process. The novelty of this work is its systematic examination of hot cracking on the compressive performance of LPBF-fabricated lattice structures. The findings will have significant implications for

the design of new cracking-free superalloys, particularly for high-temperature applications.

Keywords: Additive manufacturing; nickel-based superalloys; Hastelloy X; hot cracking; lattice structure

1. Introduction

Laser powder bed fusion (LPBF) is an advanced additive manufacturing (AM) technology that offers the ability to fabricate complex parts for a range of sectors, including medical devices and the aerospace and automotive fields [1] [2]. Nickel-based superalloys such as Hastelloy X (HX) exhibit an exceptional combination of high-temperature strength, toughness and resistance to degradation within corrosive or oxidising environments [3] [4]. For these reasons, the LPBF of HX is considered a promising technology for the manufacture of complex structural components for the gas turbine engine sector [5].

Periodic cellular lattice structures have attracted a lot of research interest due to their potential to be used in lightweight multifunctional materials and structures [6] [7] [8]. The conventional manufacturing processes that are used for the manufacture of cellular lattice structures include melt gas injection, investment casting and physical vapour deposition [9] [10] [11]. The main disadvantages of these conventional manufacturing methods lie in their high cost and inability to produce complex lattice structures [12]. For these reasons, the LPBF process is often used to fabricate various types of cellular lattice structures, such as body-centred cubic (BCC) lattice structures from 316L stainless steel [13] [14] and Ti-6Al-4V alloy [15], and BCC and face-centred cubic (FCC) cellular structures from 18Ni maraging steel and AlSi12Mg [16] [17].

To date, the focus in this area has been on the characterisation of the mechanical performance of LPBF-fabricated cellular lattice structures. For instance, Ozdemir et al. investigated the dynamic load-deformation behaviour of LPBF-fabricated Ti-6Al-4V lattice structures. Their findings showed that the lattice structures could spread impact loading in time and reduce the peak impact stress. They also observed a significant rate dependency of load-deformation characteristics [18]. Al-Saedi et al. [19] studied the deformation behaviour of Al-12Si functionally graded lattice structures and found that the collapse process occurred layer-by-layer, starting with the collapse of the lower-density layers followed by the higher-density layers in sequence. Leary et al. [20]

investigated the mechanical properties of LPBF-fabricated Inconel 625 lattice structures and found that adjustments to topology and unit cell size enabled coarse and fine tuning of the lattice's mechanical properties. They also found that IN625 lattice structures exhibited exceptional ductility, which offers the opportunity to design innovative lattice structures with unique energy-absorption characteristics. Zhang et al. [21] investigated the mechanical properties of LPBF-fabricated honeycomb pentamode Ti-6Al-4V structures, they have pointed out that the increase in strut width resulted in a transition of deformation mechanism from plastic to brittle fracture. Zargarian et al. [22] studied the effect of different factors on fatigue behaviour of additive manufactured titanium lattice structures. Their findings showed that the fatigue properties of struts have a direct effect on the fatigue strength of lattice structure and the correlation is linear. Also, when the shape of struts become more irregular, the fatigue strength of lattice structures exhibits a rapid decrease. Zhong et al. [23] studied the compressive behaviour of LPBF-fabricated lightweight 316L stainless steel tetrakaidecahedron lattice structures and found that tetrakaidekahedron structures exhibited better energy absorption performance compared to diamond and BCC structures. Also, a strong relationship between the mechanical properties and porosities of the lattice structures was disclosed in their work.

Further studies have shown that during the compressive loading of lattice structures, trusses aligned with the loading directions are the most efficient at supporting stress, while those at an incline are limited by force-resolution considerations [24] [25]. The lattice structures' failure mechanisms (including plastic yielding, elastic buckling and plastic buckling) depend on the slenderness ratio of the trusses. The slenderness ratio and relative density are interdependent: both lattice structure strength and failure mechanisms depend on the lattice's relative density and topology and the materials used to manufacture the lattice structures [6]. The LPBF of HX alloy is prone to hot cracking defects, which are related to thermally induced stresses, alloy composition, grain size and grain boundary characteristics [26] [27]. Post-treatments such as hot isostatic pressing (HIP) are commonly used to eliminate microcracks and improve the strength-ductility trade-off of as-fabricated parts [26] [28]. Although HIP processing can be used to close microcracks and improve the fatigue performance of LPBF-fabricated metallic parts [16] [29], such processing does result

in excessive grain growth and coarsening [30]. In addition, the cost of the extra post-processing reduces the economic attractiveness of the LPBF process.

Despite its theoretical and practical significance, the effect of hot cracking on the compressive performance of HX lattice structures fabricated by LPBF has yet to be explored systematically. The aim of this study is to address this knowledge gap by examining the characteristics of these microcracks and their effect on the cellular lattice structures' failure mechanism under compressive loading. The influence of minor alloying elements on hot cracking formation is also investigated.

2. Materials and procedure

2.1. Materials

This study employs two variants of Hastelloy X (HX), HX-a and HX-b, which were produced using gas atomisation with nitrogen and were provided by Sandvik Osprey (Neath, UK). HX is a Ni-Cr-Fe-Mo nickel-based superalloy that contains significant amounts of Cr, Mo, Co and Fe. The typical chemical composition of HX is shown in Table 1. HX-b contains less of the elements Si, Mn and C than HX-a; the amount of these three elements in HX-a has been measured to be 0.6% compared to the 0.2% found in HX-b. The exact amount of each minor alloying element (Si, Mn and C) in the two variants cannot be indicated for confidentiality reasons. The particle size of the two variants used in this study varied from 20 µm to 50 µm, with an average particle size of 35 µm (Fig. 1a).

Table 1.
Typical composition of HX.

Element	Cr	Fe	Mo	Co	W	Si	Mn	C	Ti	Al	Ni
wt. %	20.5–23	17–20	8–10	0.5–2.5	0.2–1	≤1	≤1	≤0.15	≤0.15	≤0.5	Bal.

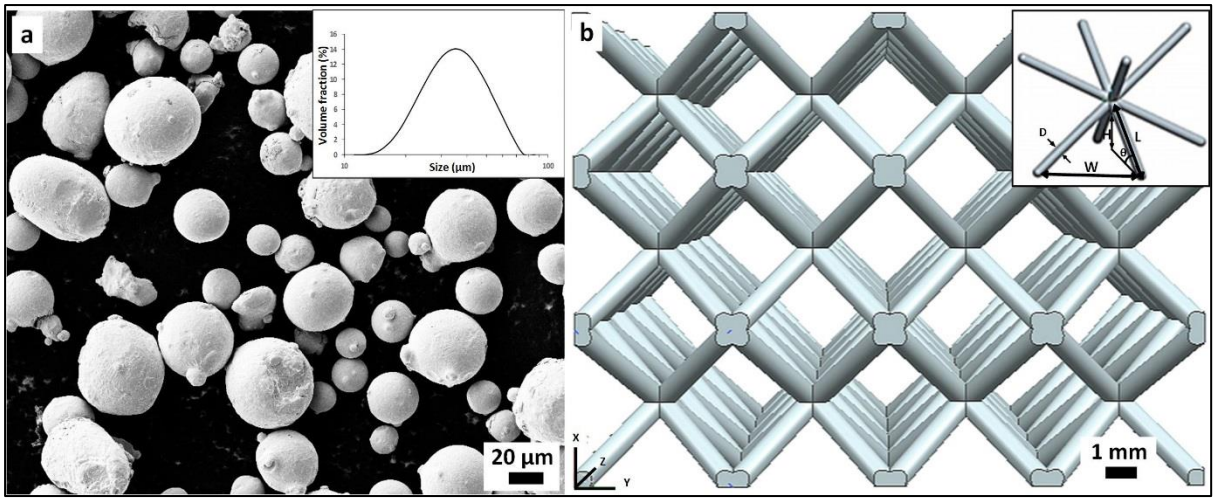

Fig. 1. Raw HX powder (a) and lattice-structure specimens for compressive testing (b).

2.2. Laser powder bed fusion and lattice structures

A Renishaw AM250 system (Renishaw Plc, UK) equipped with a modulated ytterbium fibre laser with a wavelength of 1071 nm was used to fabricate the specimens. Prior to the fabrication of the tensile and lattice specimens, a set of cubic samples was manufactured under different conditions to determine the optimum scanning speed and hatch-spacing parameters. The optimised process parameters were determined by examining the relative density of the manufactured cubic samples (10 x 10 x 10 mm^3) using the Archimedes method. The determined optimum primary process parameters for processing HX-a are as follows:

- laser power = 200 W
- layer thickness = 40 µm
- hatch spacing = 120 µm
- scanning speed = 800 mm/s

The values for HX-b are as follows:

- laser power = 200 W
- layer thickness = 40 µm
- hatch spacing = 100 µm
- scanning speed = 600 mm/s

The tensile specimens were fabricated horizontally, and their dimensions were determined on the basis of ASTM-E8/E8M-13a [31], as shown in the tensile-performance section. Although the horizontally manufactured specimens exhibited

higher tensile strength compared to the vertically fabricated parts [32], the vertical-manufacture scenario uses much more metal powder to fill the build volume. In addition, the formation and spatial distribution of the microcracks is independent of the build scenario in the LPBF of HX alloy [26]; the horizontal-manufacture scenario was thus used in the present study. The lattice-structure specimens (20 mm x 20 mm x 15 mm) used for compressive testing were designed according to a BCC-type structure, as shown in Fig. 1b [33]; the size of the cellular unit used in the study was 5 mm x 5 mm x 5 mm. The BCC cell was a 3D interaction of struts angled at 45° to the vertical. Three types of strut diameter (D = 0.5 mm, 0.75 mm and 1 mm) were used in the present work to investigate the effect of hot cracking on compressive performance. The relative density, defined as the ratio of the density of the lattice structure to the density of the solid of which it is made, is provided by the following equations [34]:

$$\bar{\rho} = (\frac{D}{L})^2 \frac{\pi}{2sin\theta cos^2\theta}[1 - (\frac{D}{L})\frac{1-\frac{1}{\pi}sin^{-1}\beta}{2\beta sin\theta cos\theta}] \qquad (1)$$

$$\beta = 1/\sqrt{1 + sin^2\theta} \qquad (2)$$

where θ and D represent the strut inclination angle (45° for BCC lattice structures, as shown in Fig. 1b) and strut diameter, respectively. L is the node-to-node strut length, and L/D is defined as the strut slenderness ratio. Fig. 2 shows the relative density $\bar{\rho}$ determined from Eq. (1) with respect to inverse slenderness D/L (L = 4.33 mm in this study).

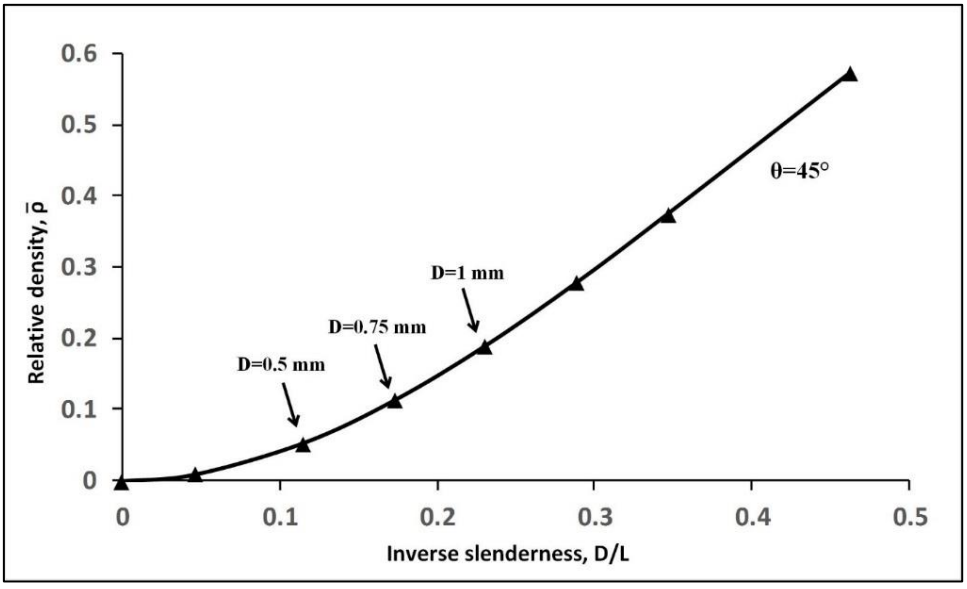

Fig. 2. Relative density with respect to inverse slenderness (5.3%, 11.3% and 18.9%).

In general, when BCC lattice structures are subjected to compressive loading, the compressive collapse strength depends upon the trusses' failure mechanisms, including plastic yielding, elastic buckling and plastic buckling. Assuming that the elastic deformation is unaffected by the growth of plasticity, the plastic-collapse strength of BCC lattice structures may be determined by [35]:

$$\sigma_{pl} = \frac{4\sqrt{2}\sigma_f}{3}\left(\frac{D}{L}\right)^3 \quad (3)$$

where σ_f denotes the flow stress of 5% strain of the parent material due to the work hardening under compressive loading. Hammetter et al. [34] have pointed out that the plastic-collapse strength decreases monotonically while the number of stacked arrays increases, whereas the effective Young's modulus remains unchanged.

2.3. Material characterisation techniques

HX-a and HX-b cubic samples were vertically sectioned parallel to the build direction, ground and then polished using standard techniques prior to optical microscopy (OM) and scanning electron microscopy (SEM) [36] [37]. The crystallographic orientation of the samples was investigated with electron backscatter diffraction (EBSD). The EBSD scanning was operated under 20 kV and was performed on an area of 1 x 1 mm^2, with a step size of 0.8 μm. Post-data processing was carried out using the HKL-EBSD Channel 5 software package. The interfaces between the grains were considered to be low-angle grain boundaries (LAGBs) when the misorientation angle was 2°–10°; otherwise, the angles were classified as high-angle grain boundaries (HAGBs). During microstructure analysis, the polished samples were electrochemically etched using oxalic acid for 10 s to reveal molten pool boundaries and solidification structures in the secondary electron (SE) SEM mode. The hot-cracking phenomenon and distribution were examined in the backscattered electron (BSD) SEM mode.

Uniaxial tensile and compressive tests were performed using a Zwick/Roell tester with a strain rate of 2 mm/min at room temperature. The engineering stress-strain curves were obtained based on two tensile specimens for each HX material.

3. Results and discussion

3.1. Microstructure and hot cracking

Fig. 3 shows the microstructure and microcracks from the side sections (parallel to the build direction) in HX-a and HX-b, where the HX-a sample contained 0.4% more minor alloying elements than HX-b. Microcracks were observed to be uniformly distributed among the hemispherical molten pools, and they penetrated to a few pre-solidified layers in the HX-a sample (Fig. 3a). The molten pools that formed were deeper and narrower in the HX-b sample compared to HX-a (Fig. 3b), which was attributed to the difference in the optimum process parameters that were employed. In particular, the determined optimum scanning speed and hatch spacing for HX-a were 800 mm/s and 120 μm, respectively, while the two values for HX-b were 600 mm/s and 100 μm, respectively. Interestingly, apart from a limited number of open pores, microcracks were not observed in the HX-b sample.

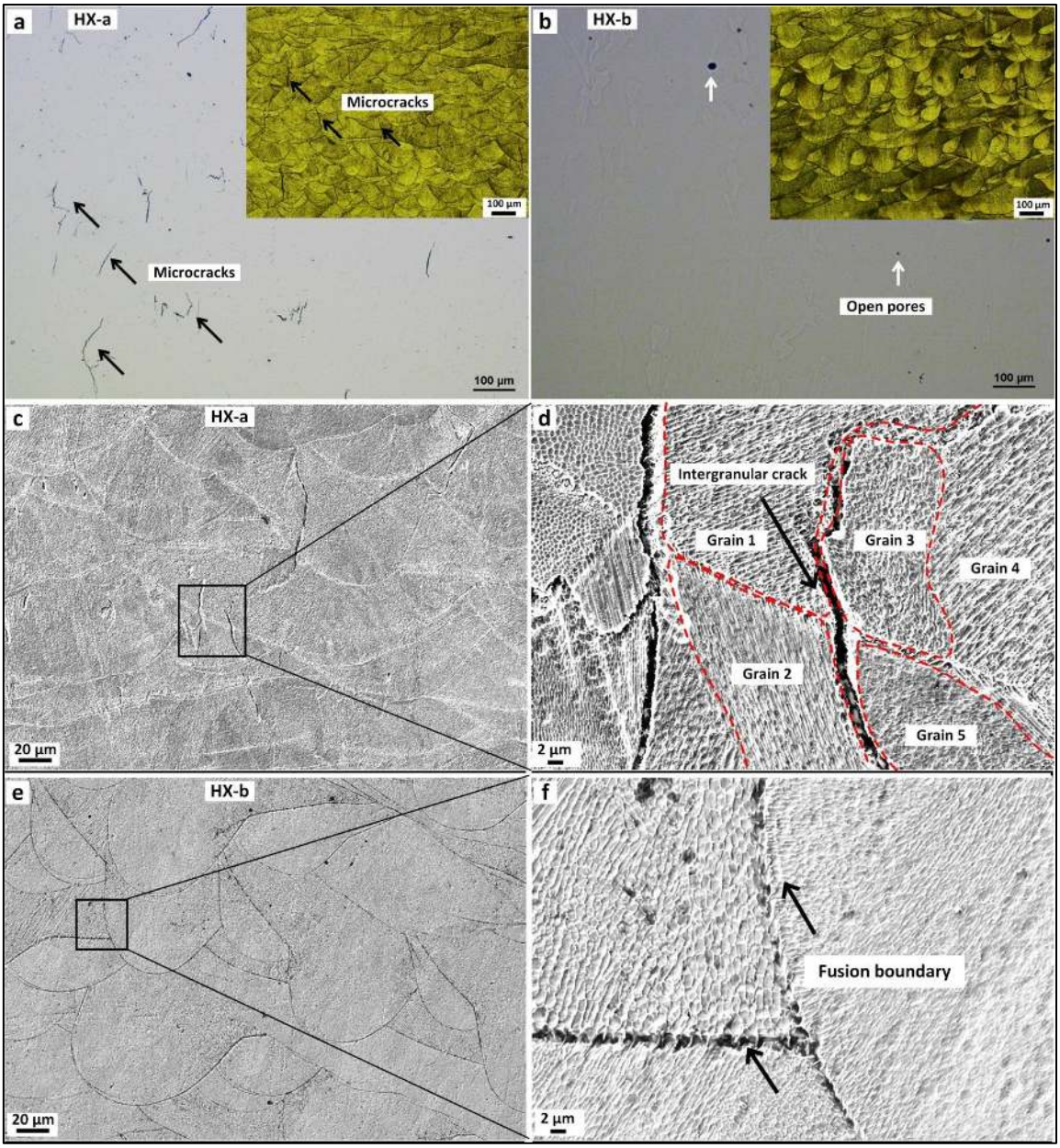

Fig. 3. Microstructure and microcracks of the as-fabricated HX samples: (a) OM images showing cracks in HX-a; (b) OM images showing microstructure and pores in HX-b; (c)–(d) SEM micrographs showing intergranular cracks in HX-a under different magnifications; (e)–(f) SEM micrographs showing microstructure of HX-b under different magnifications.

The SE-SEM micrographs revealed the solidification structure and the distribution of microcracks in HX (Fig. 3c–f). Both samples were found to exhibit typical cellular and dendritic structures following the LPBF process, which have also been reported in studies of other materials [38] [39] [40]. It should be noted that the microcracks in HX-a were surrounded by grains with different solidification features (Fig. 3d). These different solidification features indicate the grain orientations under different cooling rates, which are generally induced by the thermal gradient at the molten pools. This finding suggests that the microcracks that formed were intergranular cracks that also

propagated across pre-solidified layers. However, the microcracks were not observed under the SE-SEM mode in the HX-b sample (Fig. 3e–f), which suggests that reductions in the amount of minor alloying elements included might inhibit the formation of microcracks.

The BSD-SEM and EBSD micrographs further revealed the distribution of microcracks in the HX-a sample (Fig. 4). Figs. 4a–b show the epitaxial columnar grains formed, some of which grew across a few re-solidified layers along the build direction. Similar to the SE-SEM observations, the BSD-SEM microcracks were observed to be surrounded by different grains. In terms of the EBSD images (Fig. 4c–d), the microcracks were found to be distributed along the HAGBs (those >10°), which confirmed that the hot cracking always occurred at the HAGBs and that the microcracks that had formed were intergranular rather than transgranular cracks. This finding shows agreement with the result shown in Fig. 3d.

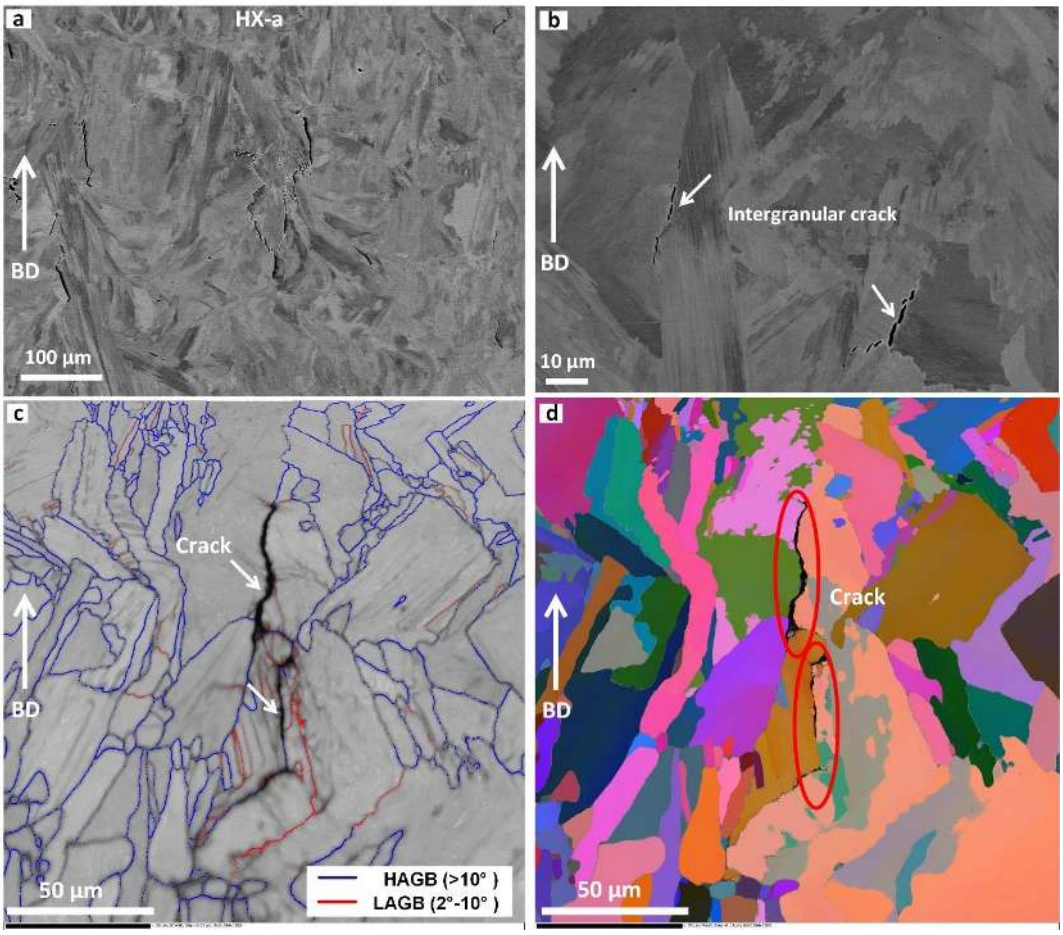

Fig. 4. Distribution of intergranular microcracks in HX-a samples: (a)-(b) BSD-SEM micrographs showing intergranular microcracks under different magnifications, (c)-(d) EBSD micrographs showing microcracks along HAGBs.

The EBSD inverse-pole figure (IPF) map and EBSD image quality (IQ) map with HAGBs and LAGBs superimposed further revealed the microstructure of the as-fabricated HX-a and HX-b samples. Epitaxial columnar grains were expected to have formed along the build direction in both samples (Fig. 5a–c). A comparison of these IPF images showed the differences in morphology and grain size of the two samples. The columnar grains were found to be nearly parallel to the build direction due to the grain growth along the positive temperature gradient. The thermal gradient along the build direction was also higher than in other directions in the molten pool, resulting in columnar grain growth during the LPBF process [41]. The grains that formed in both HX materials exhibited random crystallographic orientations instead of the strong <001> orientation, which previous studies have found to be the preferential grain-growth orientation for FCC structure materials [42] [43].

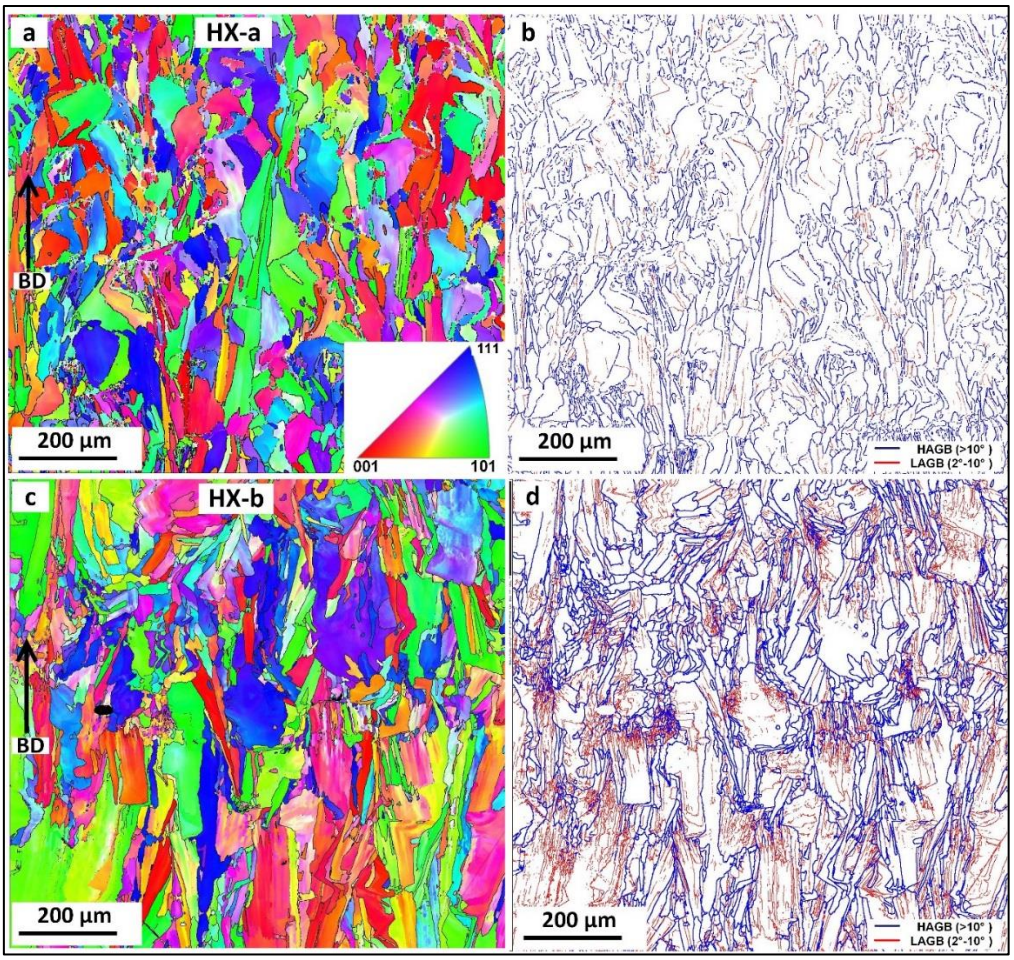

Fig. 5. EBSD images of the as-fabricated HX samples: (a)–(b) HX-a sample; (c)–(d) HX-b sample.

Interestingly, the fraction of LAGBs increased from 36% in the HX-a sample to 52% in the HX-b sample. Considering the difference in the chemical composition, the 16%

increase in LAGBs may have been attributable to the reduction of the minor alloying elements in HX-b, particularly the carbon element. Although carbon generally contributes to the formation of carbides with the reaction of the Mo and Cr elements – which helps to control the grain size and increases resistance to grain-boundary sliding [44] [5] – this kind of segregation makes nickel-based superalloys more susceptible to hot cracking [45]. This scenario is in agreement with Fig. 3, which shows no microcracks in the HX-b sample. The hot cracking was eliminated in HX-b because the increased LAGBs made the accumulated residual thermal stresses uniform and strengthened the boundaries' cohesion. The reduction in the carbides that formed could have degraded the mechanical strength of HX-b compared to HX-a; this will be examined in the next section.

The EDX mapping further revealed the chemical composition of the as-fabricated HX-a, particularly the hot cracking zone (Fig. 6). Mo-rich carbides were detected along the microcracks, which were formed at the HAGBs. This finding confirms that element segregation occurred at the grain boundaries during the rapid solidification process. Indeed, element segregation in the LPBF of HX has also been reported in previous studies, where Mo-rich M_6C and Cr-rich $M_{23}C_6$ carbides were found to have formed at the microcracks [27] [46]. Cr-rich carbides were not detected in the present work, which may have been because the process parameters that were employed offered insufficient time for $M_{23}C_6$ carbide precipitation. Mo-rich carbides were also detected at the cellular and columnar solidification walls in the HX-b sample, in which hot cracking was not observed, implying that element segregation may not be the only contributor to hot cracking during the LPBF of HX alloys.

It should be noted that the hot cracking formation mechanism in additive manufacturing of HX is different from that of other brittle materials. This is because within the additive manufacturing of HX, segregated carbides are unable to fully dissolve into the surrounding matrix under the rapid heating; partial dissolution occurs and a low melting point eutectic liquid film forms at the grain boundary region. Hot cracks may form when the accumulated thermal residual stresses pull on the liquid film on the grain boundary. While the cracks in brittle materials generally start from a high localised stress concentration [47]. Based on the authors' findings, an effective method to restrain cracks in additive manufacturing of HX is to reduce the amount of carbon element in order to reduce the carbide segregation; another possible method

would be the introduction of nanoscale nucleation agent, which promotes the heterogeneous nucleation and uniforms the strain that is induced by the residual stress accumulation. This technique has been successfully employed to mitigate the hot cracking in 3D printing of high-strength aluminium alloys (Al 6061 and 7075 series) [48]. The two methods could be used in conventional processing such as in joining, casting and injection moulding, in which hot cracking is also a common issue, but they may not be useful for brittle materials since the crack origin mechanism is different.

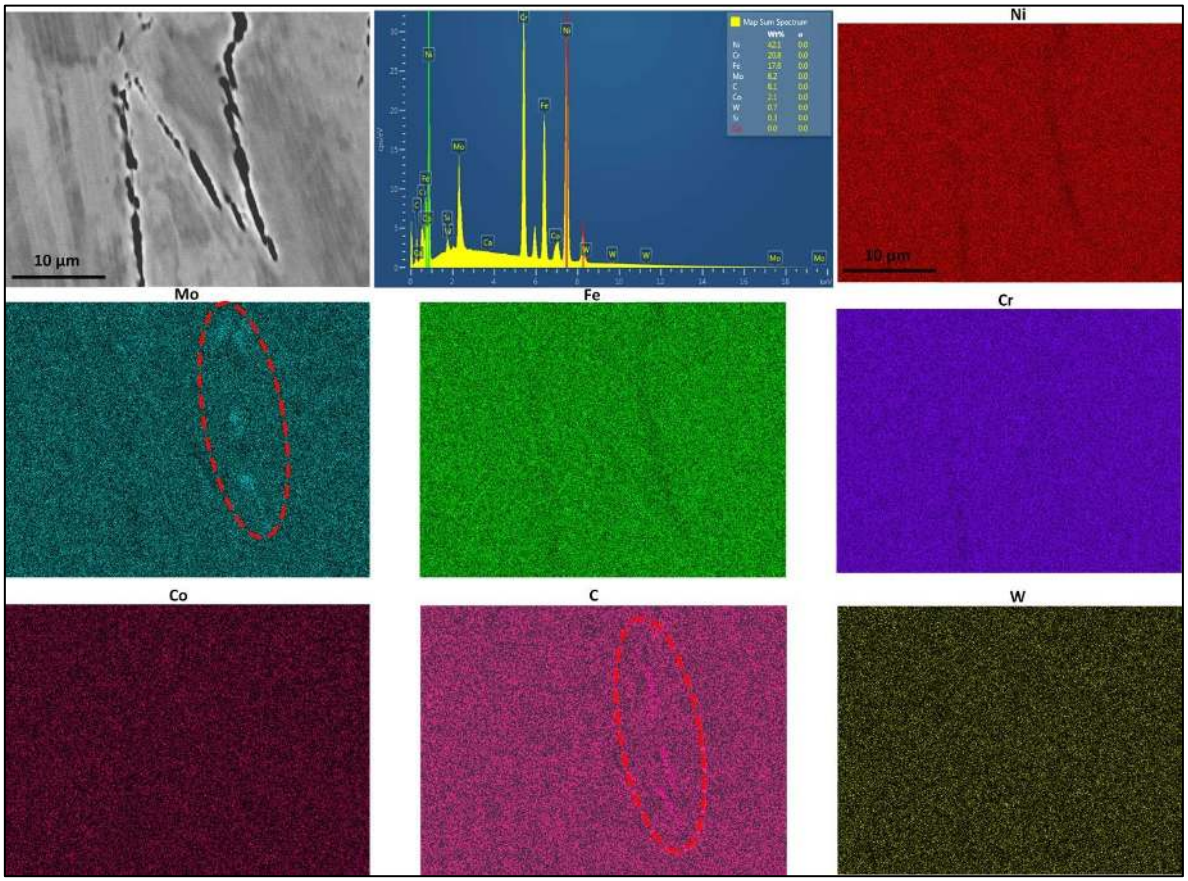

Fig. 6. EDX mapping of the crack zone from the HX-a sample.

3.2. Mechanical performance

3.2.1. Tensile performance

Fig. 7 shows the tensile-testing results of the as-fabricated HX-a and HX-b specimens and their dimensions. The two specimens (called HX-a-1 and HX-a-2) were used to obtain the stress-strain curves for HX-a, while HX-b-1 and HX-b-2 were used for HX-b material. The tensile performances of the two specimens for both cases were found to be consistent. The yield strength and elongation were determined to be 730 ± 2 MPa and 14 ±1% for the HX-a specimens and 590 ± 5 MPa and 37±2% for the

HX-b samples, respectively. The HX-b specimens also exhibited a more apparent necking phenomenon compared to the HX-a specimens. The HX-a specimens exhibited lower ductility because of the microcracks that formed; this was not surprising, since the microcracks acted as stress-concentration sites and were detrimental to various mechanical properties [49] [26]. Compared to HX-a, the HX-b specimens offered roughly 140 MPa lower yield strength and 23% higher elongation, respectively. Considering the small difference in the chemical composition, the reduction of carbon content might result in the formation of fewer carbides in HX-b specimens. The carbides are usually located at the grain boundaries and form directly from the liquid during rapid solidification at high temperatures [50]. Carbides play a significant role in strengthening the grain boundaries and increasing the resistance to grain-boundary sliding, thus improving the tensile strength. This behaviour explains the reduction of tensile strength found in the HX-b specimens compared to the HX-a specimens. Table 2 shows the tensile testing results and the parameters of the lattice structures used in the compressive analysis.

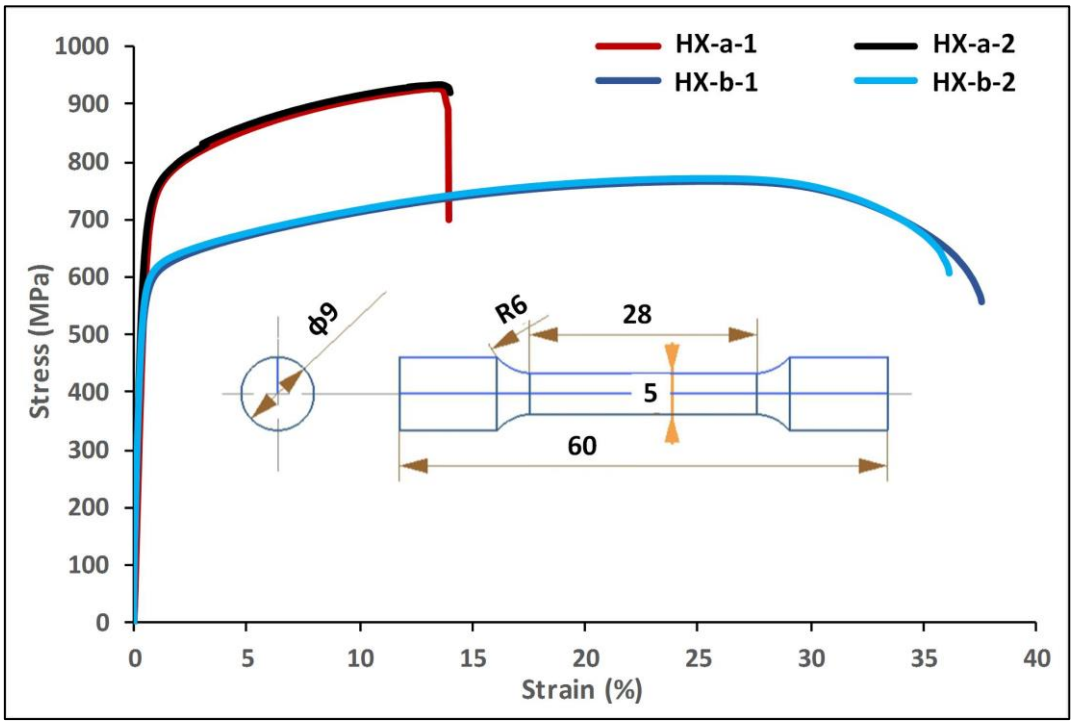

Fig. 7. Tensile performance of the as-fabricated HX specimens.

Table 2

Tensile test results of the as-fabricated HX-a and HX-b samples.

Category	$D\ (mm)$	$\bar{\rho}$	$\sigma_o\ (MPa)$	$\sigma_f\ (MPa)$	$\sigma_o \cdot \bar{\rho}\ (MPa)$

HX-a (with cracking)	0.5	0.053	730 ± 2	850 ± 5	38.98
	0.75	0.113	730 ± 2	850 ± 5	82.78
	1	0.189	730 ± 2	850 ± 5	138.63
HX-b (cracking free)	0.5	0.053	590 ± 5	670 ± 3	31.5
	0.75	0.113	590 ± 5	670 ± 3	66.9
	1	0.189	590 ± 5	670 ± 3	112

Fig. 8 shows the fracture surfaces of both the as-fabricated HX-a (Fig. 8a) and HX-b (Fig. 8b) samples following the tensile testing. The microcracks in HX-a further opened to some degree under uniaxial loading. A few cleavage-like fracture surfaces were observed in the HX-a samples, indicating brittle fracture behaviour with low ductility. This fracture behaviour differed from that found in the authors' previous study, in which some elongated columnar grains with a dendritic structure were observed in the fracture surface, resulting in 40% elongation. This finding might be attributable to the difference in the build and loading directions. The build direction was parallel to the uniaxial loading direction described in a previous study [26], while the two directions were perpendicular in the present work. Compared to HX-a alloy, a more apparent necking and a few opened pores were observed in HX-b, while opened cracks were not observed (Fig. 8b). Fewer cleavage-like surfaces were observed in HX-b compared to HX-a, indicating a more ductile fracture behaviour in the former, as supported by the determined strain in the engineering stress-strain curves shown in Fig. 7.

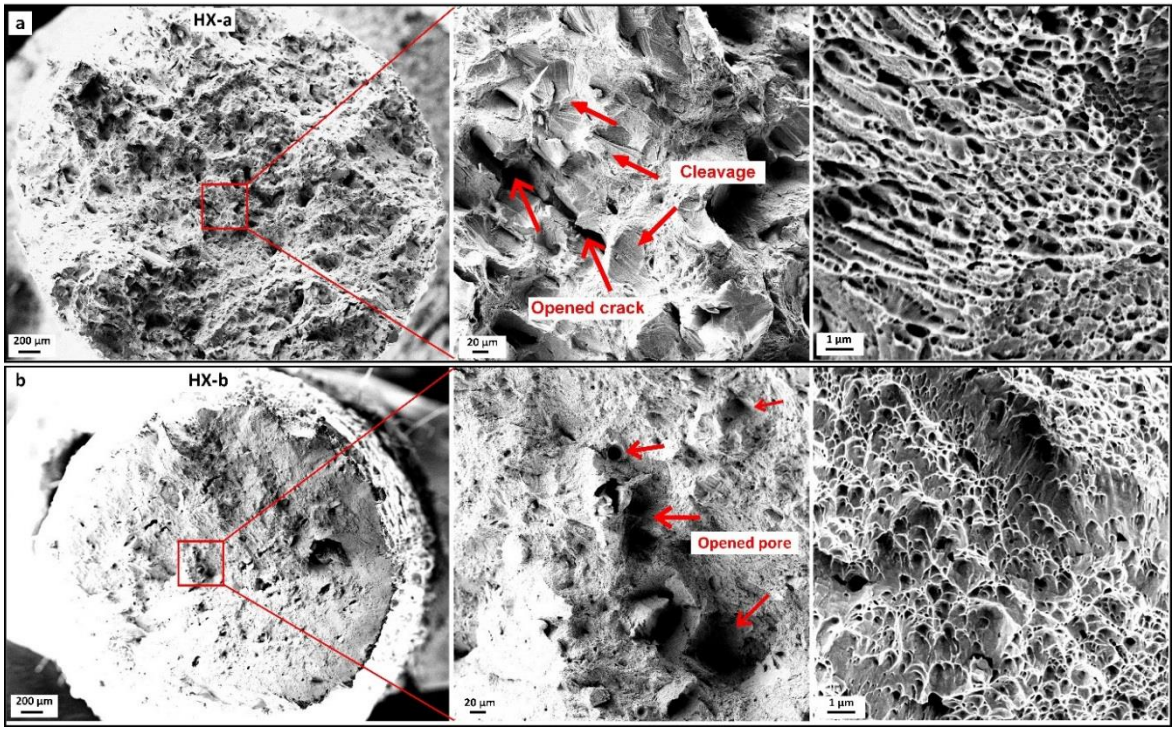

Fig. 8. Fracture surface of the HX specimens after tensile testing.

3.2.2. Compressive performance and failure mechanism

Fig. 9 shows the as-fabricated HX-a lattice structures with three different strut diameters (0.5 mm, 0.75 mm and 1 mm) during compressive testing. The shape and structure of the HX-b lattice specimens were similar to those of the HX-b specimens and thus are not shown in Fig. 9. Since the microstructure analysis qualitatively demonstrated the distribution of microcracks in HX-a and open pores in HX-b, the lattice specimens were not further examined with micro-CT to detect the defects, but the strut size was measured by SEM. The SEM-measured strut size was found to be slightly larger than the predefined size due to the formation of dross (Fig. 9a–c) defects in every case. Both the size and number of the pieces of dross tended to increase with strut size. This phenomenon was also observed in the LPBF of overhang structures [51] [52].

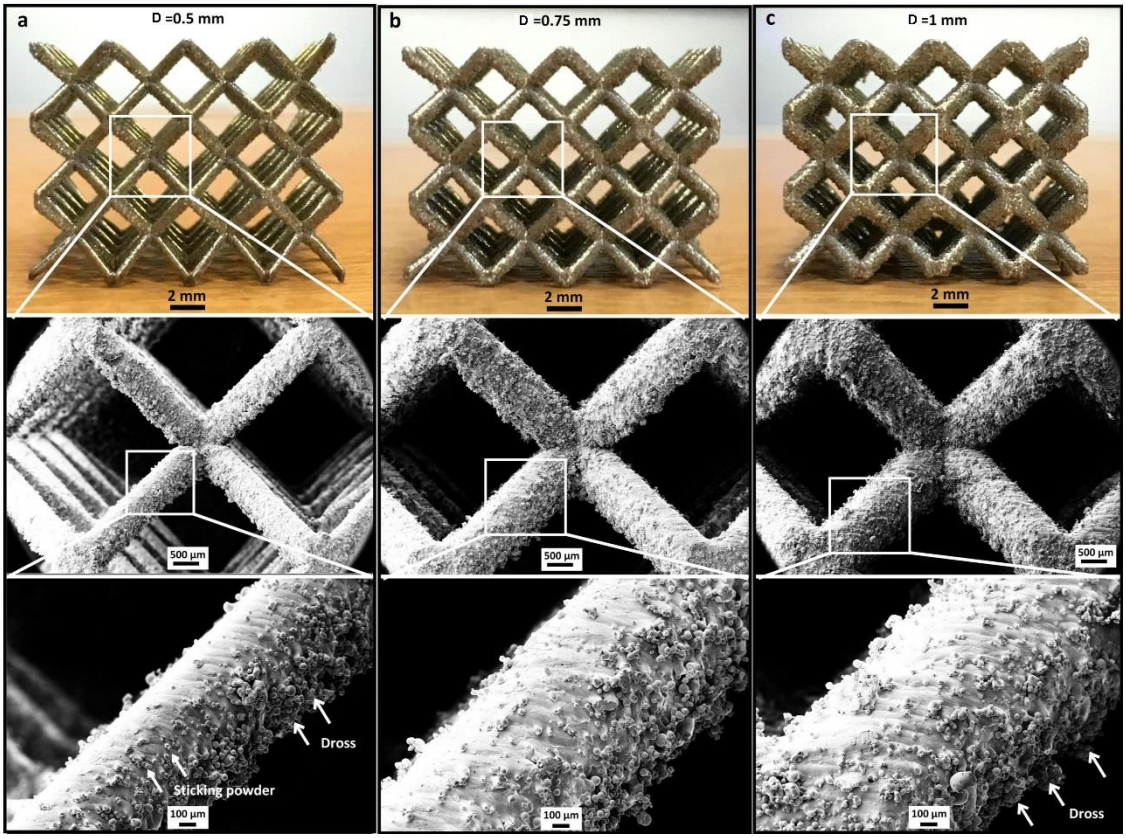

Fig. 9. LPBF-fabricated lattice specimens with different strut sizes.

Fig. 10 shows the theoretically calculated and experimentally obtained plastic-collapse strengths of LPBF-fabricated lattice structures after compressive testing. Both the calculated and experimentally measured collapse strength values were found to have increased with larger strut sizes; the strength value varied from 3 MPa to 20 MPa when the strut size changed from 0.5 mm to 1 mm, which implies that the experimental measurement was consistent with the theoretical calculation. The collapse strength of HX-a (with cracking) was found to be higher than HX-b (cracking free) under each strut size; this trend was more apparent with larger strut sizes, suggesting that the plastic-collapse strength is sensitive to the size of lattice structure strut. Note that the theoretical plastic-collapse strength is based on the assumption that elastic deformation will be unaffected by the growth of plasticity, which means that this estimation is only suitable for those BCC lattice structures whose failure mode is controlled by plastic yielding. This indicates that when BCC lattice structures are subjected to compressive testing under different failure mechanisms, the plastic-collapse strength might not be the only indicator to describe the lattice structures' compressive response.

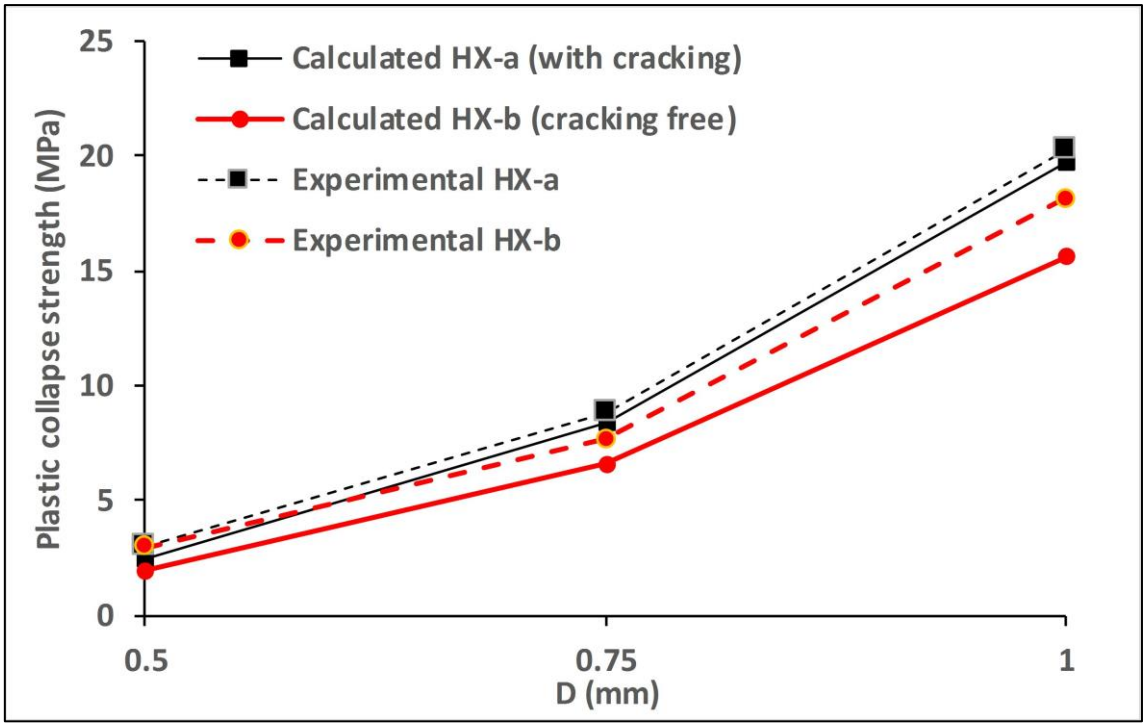

Fig. 10. The calculated and experimentally obtained collapse strength of both HX-a and HX-b alloys under different strut sizes.

Fig. 11 shows the compressive performance of both HX-a and HX-b lattice specimens with different strut sizes (i.e. relative density). The non-dimensional compressive strengths $\sigma/(\sigma_o\bar{\rho})$ with respect to nominal strain are plotted in Fig. 11a; this non-dimensional measure of strength is an indicator of the efficiency of the load-carrying capability of the lattice structure. As the figure shows, increased strut diameters resulted in increased initial compressive peak strengths in both cases, but the HX-b (cracking-free) case showed overall higher strength values compared to the HX-a (with cracking) case. This trend was more apparent with increased strut sizes. The collapse strength increased from 0.08 to 0.14 for HX-a under the three strut sizes, while the values varied from 0.1 to 0.16 for HX-b lattice structures.

The compressive responses of both HX-a-1mm and HX-b-1mm specimens are detailed in Fig. 11b to provide a better understanding of the effect of cracking on lattice structure failure.

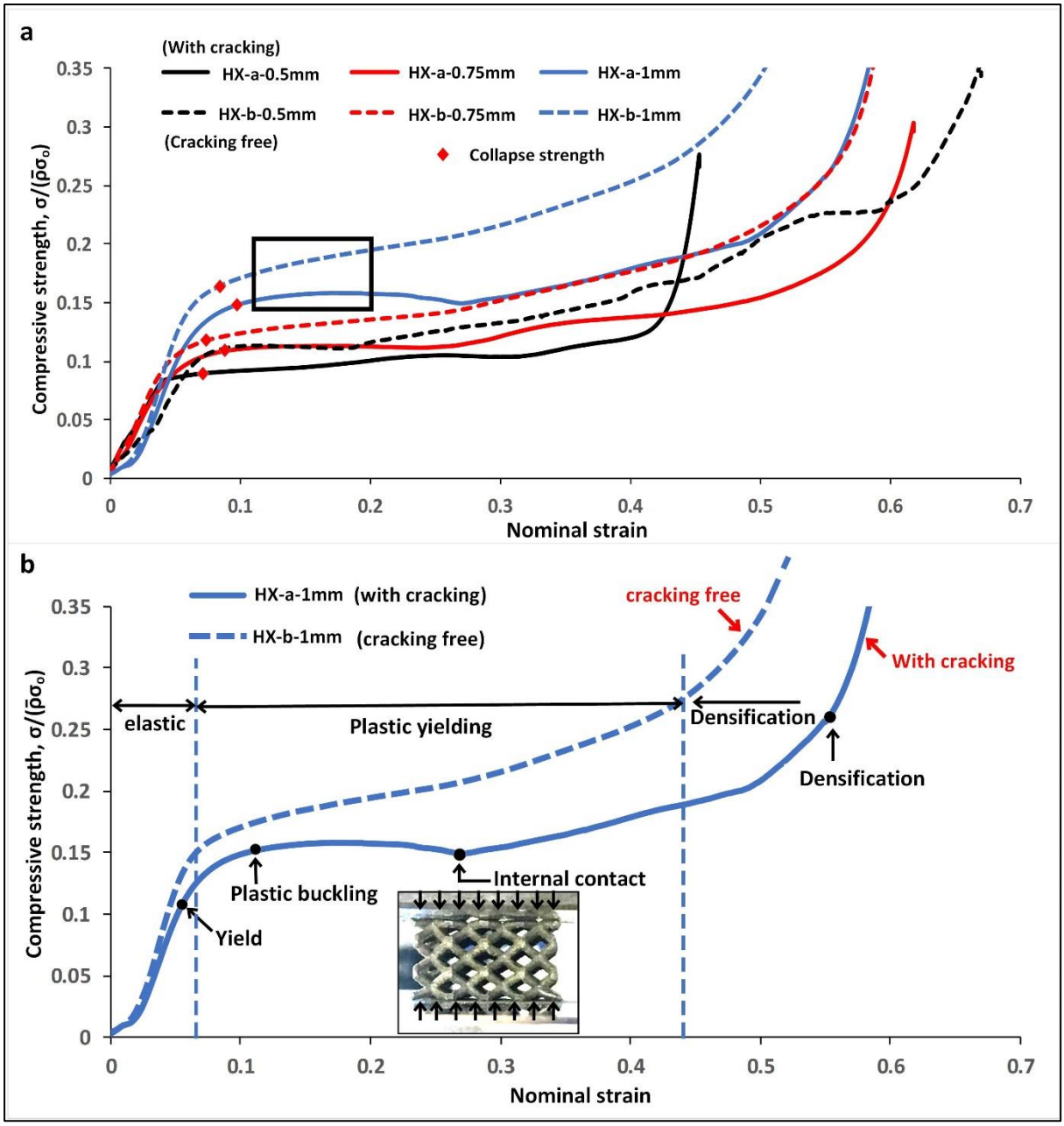

Fig. 11. Compressive performance of both the cracking-free and with-cracking lattice specimens with different strut sizes.

As Fig. 11b shows, three distinct responses were observed in the case of HX-b-1mm (cracking free). The linear elastic response occurred after the initial bedding-in stage, which is a similar behaviour to many other cellular metals [53] [54]. Following the linear response, plasticity and strain hardening took place, which led to a monotonically increasing flow stress until densification occurred, at which point the lattice structure exhibited greater load resistance. For the HX-a-1mm (with-cracking) lattice structure, the stress-strain response diverged from being linear (marked as 'Yield' in the curve in the figure) as plasticity developed within the nodal regions. The

accompanying increase in the nodal cross-sectional area resulted in geometric hardening: the strength continued to rise to a certain level, at which point the still-elastic struts buckled and the load started to drop (marked as 'Plastic buckling' in the figure). During the plastic buckling, strain softening continued until, at a strain of about 0.27, internal contact occurred between the struts, and the stress began to rise. Densification took place at a strain of about 0.56.

When the structure size was fixed at 1 mm, the lattice structure that showed cracking exhibited an overall lower compressive strength compared to the cracking-free lattice structure, which may be attributable to the plastic buckling induced by the cracking in the HX-a-1mm lattice structure. In contrast, the HX-b samples exhibited a 99.5% relative density without cracking; the 0.5% porosity was found to have had no apparent influence on plastic buckling under compressive loading. Extensive work on the study of lattice structures' compressive performance has reported that strain hardening is followed by the onset of plastic buckling; the plastic buckling is then followed by softening, which depends to a large extend on the slenderness ratio [55]. In the present study, when the slenderness ratio was fixed, plastic buckling only occurred in the with-cracking HX lattice structures under different relative densities, which suggests that the cracking was also a significant factor in plastic buckling. The experimental findings have also revealed that the failure mechanism for the cracking-free HX lattice structures was controlled by plastic yielding, while the failure mode of the HX lattice structures with hot cracking was controlled by plastic buckling.

Fig. 12 shows typical micrographs of the lattice specimens after compression. Fracture sites were observed in the HX-a-0.5mm and HX-a-1mm samples (Fig. 12a and c), both of which suffered from hot cracking. Since the microcracks were uniformly distributed in the as-fabricated HX-a lattice structures (Fig. 3), the fracture occurred more easily at the node positions (Fig. 12c), suggesting that stress-concentration sites are more likely to fail compared to other positions under compressive loading. The densified HX-b lattice structures with 0.5 mm and 1 mm structure sizes are shown in Fig. 12a and d, respectively. Interestingly, fracturing was not observed in the node positions of the HX-b structures, which implies that the HX-b lattice structures were subjected to plastic yielding and hardening during the post-elastic stage until densification occurred under the compressive load. This finding explains the monotonic increase in strength with respect to nominal strain shown in Fig. 11.

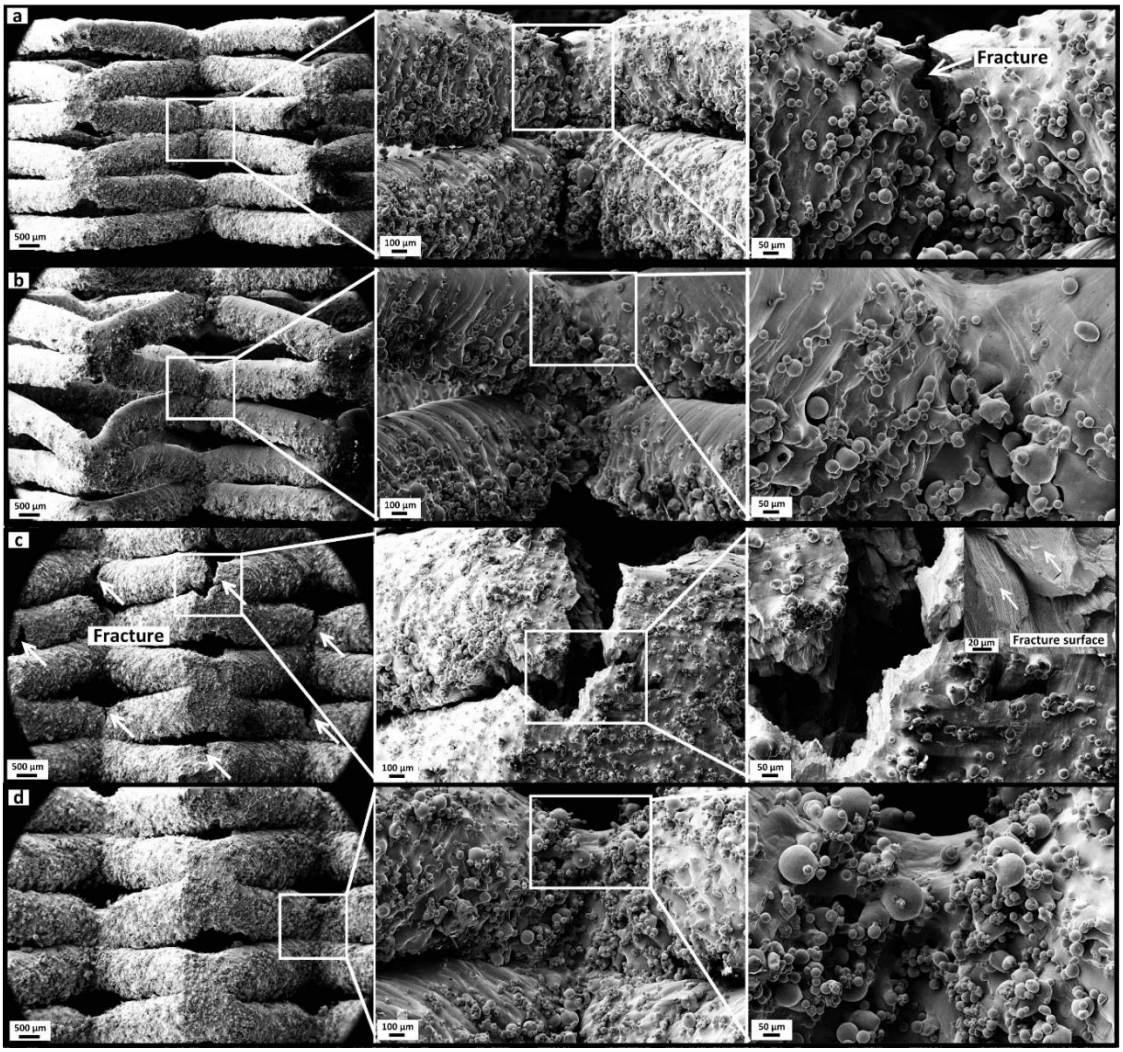

Fig. 12. SEM micrographs showing the lattice specimens after compressive testing: (a) HX-a-0.5 mm; (b) HX-b-0.5 mm; (c) HX-a-1 mm; (d) HX-b-1 mm.

4. Conclusions

This study has investigated the effects of minor alloying elements on hot-cracking formation and the influences of hot cracking on the mechanical properties of Hastelloy X fabricated via laser powder bed fusion. The materials' compressive performance in particular was examined for the first time in this work. This study has also compared the lattice structures of two Hastelloy X materials' collapse mechanisms under compressive loading. The following findings were derived from the experimental results.

(1) A reduction in the amount of minor alloying elements, such as Si, Mn and C, enabled the elimination of microcracks in the LPBF-manufactured HX specimens. This reduction, however, also resulted in about 140 MPa lower yield

strength and 23% higher elongation compared to the HX specimens that did not experience hot cracking.

(2) The microcracks were found to be uniformly distributed in the as-fabricated HX samples along the high-angle grain boundaries, thus indicating that the hot cracks were intergranular. Mo-rich carbides were examined to be segregated at the crack sites.

(3) The measured initial peak compressive strength increased with an increase in the strut sizes (i.e. relative density) in both the HX-a and HX-b cases, but the cracking-free HX-b exhibited overall higher values compared to the with-cracking HX-a alloy.

(4) For the cracking-free HX-b alloy, the lattice structures' failure mechanism was found to be controlled by plastic yielding, while the failure of the HX-a lattice structures was dominated by the plastic buckling that occurred due to the microcracks formed during the LPBF process.

These results indicate that microcracking defects in the additive manufacturing of Hastelloy X can be mitigated by reducing the amount of minor alloying elements that are included, although doing so would degrade the mechanical strength after the LPBF process. Under compressive loading, the cracking-free HX lattice structures failed because of plastic yielding, while the failure mechanism of the with-cracking HX lattice structures was primarily plastic buckling. Compared to the tensile specimens, the lattice structures had much thinner struts, which may have resulted in different cooling rates and grain sizes within the LPBF process. Further study will be necessary to investigate the molten pool dynamics involved in the manufacture of lattice structures. Future work will also focus on the elimination of hot cracking while maintaining high mechanical strength and elongation after the LPBF process.

Acknowledgements

The research was conducted within the framework of ASTUTE 2020, a joint collaborative project of Cardiff University and Swansea University, UK, funded by European Regional Development through the Welsh Government and the participating Higher Education Institutions.

References

[1] N. Guo, M.C. Leu, Additive manufacturing: Technology, applications and research

needs, Front. Mech. Eng. 8 (2013) 215–243. doi:10.1007/s11465-013-0248-8.

[2] S.H. Huang, P. Liu, A. Mokasdar, L. Hou, Additive manufacturing and its societal impact: A literature review, Int. J. Adv. Manuf. Technol. 67 (2013) 1191–1203. doi:10.1007/s00170-012-4558-5.

[3] T.M. Pollock, S. Tin, Nickel-Based Superalloys for Advanced Turbine Engines: Chemistry, Microstructure and Properties, J. Propuls. Power. 22 (2006) 361–374. doi:10.2514/1.18239.

[4] Q. Han, H. Gu, R. Setchi, Discrete element simulation of powder layer thickness in laser additive manufacturing, Powder Technol. 352 (2019) 91–102. doi:10.1016/j.powtec.2019.04.057.

[5] M.M. Attallah, R. Jennings, X. Wang, L.N. Carter, Additive manufacturing of Ni-based superalloys: The outstanding issues, MRS Bull. 41 (2016) 758–764. doi:10.1557/mrs.2016.211.

[6] H.N.G. Wadley, N.A. Fleck, A.G. Evans, Fabrication and structural performance of periodic cellular metal sandwich structures, Compos. Sci. Technol. 63 (2003) 2331–2343. doi:10.1016/S0266-3538(03)00266-5.

[7] C. Qiu, S. Yue, N.J.E. Adkins, M. Ward, H. Hassanin, P.D. Lee, P.J. Withers, M.M. Attallah, Influence of processing conditions on strut structure and compressive properties of cellular lattice structures fabricated by selective laser melting, Mater. Sci. Eng. A. 628 (2015) 188–197. doi:10.1016/j.msea.2015.01.031.

[8] Y. Liu, J. Zhang, Y. Yang, J. Li, J. Chen, Study on the influence of process parameters on the clearance feature in non-assembly mechanism manufactured by selective laser melting, J. Manuf. Process. 27 (2017) 98–107. doi:10.1016/j.jmapro.2017.04.005.

[9] J. Banhart, Manufacture, characterisation and application of cellular metals and metal foams, Prog. Mater. Sci. 46 (2001) 559–632. doi:10.1016/S0079-6425(00)00002-5.

[10] J. Wang, A.G. Evans, K. Dharmasena, H.N.G. Wadley, On the performance of truss panels with Kagomé cores, Int. J. Solids Struct. 40 (2003) 6981–6988. doi:10.1016/S0020-7683(03)00349-4.

[11] F.W. Zok, S.A. Waltner, Z. Wei, H.J. Rathbun, R.M. McMeeking, A.G. Evans, A protocol for characterizing the structural performance of metallic sandwich panels: Application to pyramidal truss cores, Int. J. Solids Struct. 41 (2004) 6249–6271. doi:10.1016/j.ijsolstr.2004.05.045.

[12] I. Maskery, N.T. Aboulkhair, A.O. Aremu, C.J. Tuck, I.A. Ashcroft, R.D. Wildman, R.J.M. Hague, A mechanical property evaluation of graded density Al-Si10-Mg lattice structures manufactured by selective laser melting, Mater. Sci. Eng. A. 670 (2016) 264–274. doi:10.1016/j.msea.2016.06.013.

[13] S. McKown, Y. Shen, W.K. Brookes, C.J. Sutcliffe, W.J. Cantwell, G.S. Langdon, G.N. Nurick, M.D. Theobald, The quasi-static and blast loading response of lattice structures, Int. J. Impact Eng. 35 (2008) 795–810. doi:10.1016/j.ijimpeng.2007.10.005.

[14] Y. Liu, Z. Pang, J. Zhang, Comparative study on the influence of subsequent thermal cycling on microstructure and mechanical properties of selective laser melted 316L stainless steel, Appl. Phys. A Mater. Sci. Process. 123 (2017) 688. doi:10.1007/s00339-017-1313-7.

[15] S.L. Campanelli, N. Contuzzi, A.D. Ludovico, F. Caiazzo, F. Cardaropoli, V. Sergi, Manufacturing and characterization of Ti6Al4V lattice components manufactured by selective laser melting, Materials (Basel). 7 (2014) 4803–4822.

doi:10.3390/ma7064803.

[16] N. Contuzzi, S.L. Campanelli, C. Casavola, L. Lamberti, Manufacturing and characterization of 18Ni marage 300 lattice components by selective laser melting, Materials (Basel). 6 (2013) 3451–3468. doi:10.3390/ma6083451.

[17] M. Leary, M. Mazur, J. Elambasseril, M. McMillan, T. Chirent, Y. Sun, M. Qian, M. Easton, M. Brandt, Selective laser melting (SLM) of AlSi12Mg lattice structures, Mater. Des. (2016). doi:10.1016/j.matdes.2016.02.127.

[18] Z. Ozdemir, E. Hernandez-Nava, A. Tyas, J.A. Warren, S.D. Fay, R. Goodall, I. Todd, H. Askes, Energy absorption in lattice structures in dynamics: Experiments, Int. J. Impact Eng. 89 (2016) 49–61. doi:10.1016/j.ijimpeng.2015.10.007.

[19] D.S.J. Al-Saedi, S.H. Masood, M. Faizan-Ur-Rab, A. Alomarah, P. Ponnusamy, Mechanical properties and energy absorption capability of functionally graded F2BCC lattice fabricated by SLM, Mater. Des. 144 (2018) 32–44. doi:10.1016/j.matdes.2018.01.059.

[20] M. Leary, M. Mazur, H. Williams, E. Yang, A. Alghamdi, B. Lozanovski, X. Zhang, D. Shidid, L. Farahbod-Sternahl, G. Witt, I. Kelbassa, P. Choong, M. Qian, M. Brandt, Inconel 625 lattice structures manufactured by selective laser melting (SLM): Mechanical properties, deformation and failure modes, Mater. Des. 157 (2018) 179–199. doi:10.1016/j.matdes.2018.06.010.

[21] L. Zhang, B. Song, A. Zhao, R. Liu, L. Yang, Y. Shi, Study on mechanical properties of honeycomb pentamode structures fabricated by laser additive manufacturing: Numerical simulation and experimental verification, Compos. Struct. 226 (2019) 111199. doi:10.1016/j.compstruct.2019.111199.

[22] A. Zargarian, M. Esfahanian, J. Kadkhodapour, S. Ziaei-Rad, D. Zamani, On the fatigue behavior of additive manufactured lattice structures, Theor. Appl. Fract. Mech. 100 (2019) 225–232. doi:10.1016/j.tafmec.2019.01.012.

[23] T. Zhong, K. He, H. Li, L. Yang, Mechanical properties of lightweight 316L stainless steel lattice structures fabricated by selective laser melting, Mater. Des. 181 (2019) 108076. doi:10.1016/j.matdes.2019.108076.

[24] T.M. McCormack, R. Miller, O. Kesler, L.J. Gibson, Failure of sandwich beams with metallic foam cores, Int. J. Solids Struct. 38 (2001) 4901–4920. doi:10.1016/S0020-7683(00)00327-9.

[25] H. Bart-Smith, J.W. Hutchinson, N.A. Fleck, A.G. Evans, Influence of imperfections on the performance of metal foam core sandwich panels, Int. J. Solids Struct. 39 (2002) 4999–5012. doi:10.1016/S0020-7683(02)00250-0.

[26] Q. Han, R. Mertens, M. Montero-Sistiaga, S. Yang, R. Setchi, K. Vanmeensel, B. Hooreweder, S.L. Evans, H. Fan, Laser powder bed fusion of Hastelloy X: effects of hot isostatic pressing and the hot cracking mechanism, Mater. Sci. Eng. A. 732 (2018) 228–239. doi:https://doi.org/10.1016/j.msea.2018.07.008.

[27] G. Marchese, G. Basile, E. Bassini, A. Aversa, M. Lombardi, D. Ugues, P. Fino, S. Biamino, Study of the microstructure and cracking mechanisms of hastelloy X produced by laser powder bed fusion, Materials (Basel). 11 (2018) 106. doi:10.3390/ma11010106.

[28] D. Tomus, Y. Tian, P.A. Rometsch, M. Heilmaier, X. Wu, Influence of post heat treatments on anisotropy of mechanical behaviour and microstructure of Hastelloy-X parts produced by selective laser melting, Mater. Sci. Eng. A. 667 (2016) 42–53. doi:10.1016/j.msea.2016.04.086.

[29] M.W. Wu, J.K. Chen, B.H. Lin, P.H. Chiang, Improved fatigue endurance ratio of

additive manufactured Ti-6Al-4V lattice by hot isostatic pressing, Mater. Des. 134 (2017) 163–170. doi:10.1016/j.matdes.2017.08.048.

[30] C. De Formanoir, S. Michotte, O. Rigo, L. Germain, S. Godet, Electron beam melted Ti-6Al-4V: Microstructure, texture and mechanical behavior of the as-built and heat-treated material, Mater. Sci. Eng. A. 652 (2016) 105–119. doi:10.1016/j.msea.2015.11.052.

[31] Standard Test Methods for Tension Testing of Metallic Materials, (n.d.). https://compass.astm.org/Standards/HISTORICAL/E8E8M-13A.htm (accessed September 15, 2018).

[32] C. Qiu, N.J.E. Adkins, M.M. Attallah, Selective laser melting of Invar 36: Microstructure and properties, Acta Mater. (2016). doi:10.1016/j.actamat.2015.10.020.

[33] Q. Feng, Q. Tang, Y. Liu, R. Setchi, S. Soe, S. Ma, L. Bai, Quasi-static analysis of mechanical properties of Ti6Al4V lattice structures manufactured using selective laser melting, Int. J. Adv. Manuf. Technol. 94 (2018) 2301–2313. doi:10.1007/s00170-017-0932-7.

[34] C.I. Hammetter, R.G. Rinaldi, F.W. Zok, Pyramidal Lattice Structures for High Strength and Energy Absorption, J. Appl. Mech. 80 (2013) 041015. doi:10.1115/1.4007865.

[35] K. Ushijima, W.J. Cantwell, R.A.W. Mines, S. Tsopanos, M. Smith, An investigation into the compressive properties of stainless steel micro-lattice structures, J. Sandw. Struct. Mater. 13 (2011) 303–329. doi:10.1177/1099636210380997.

[36] Q. Han, R. Setchi, S.L. Evans, Synthesis and characterisation of advanced ball-milled Al-Al2O3 nanocomposites for selective laser melting, Powder Technol. 297 (2016) 183–192. doi:10.1016/j.powtec.2016.04.015.

[37] Q. Han, R. Setchi, F. Lacan, D. Gu, S.L. Evans, Selective laser melting of advanced Al-Al2O3 nanocomposites: Simulation, microstructure and mechanical properties, Mater. Sci. Eng. A. 698 (2017) 162–173. doi:10.1016/j.msea.2017.05.061.

[38] Q. Han, Y. Jiao, Effect of heat treatment and laser surface remelting on AlSi10Mg alloy fabricated by selective laser melting, Int. J. Adv. Manuf. Technol. 102 (2019) 3315–3324. doi:10.1007/s00170-018-03272-y.

[39] H. Gong, K. Rafi, H. Gu, G.D. Janaki Ram, T. Starr, B. Stucker, Influence of defects on mechanical properties of Ti-6Al-4V components produced by selective laser melting and electron beam melting, Mater. Des. (2015). doi:10.1016/j.matdes.2015.07.147.

[40] Q. Han, Y. Geng, R. Setchi, F. Lacan, D. Gu, S.L. Evans, Macro and nanoscale wear behaviour of Al-Al2O3 nanocomposites fabricated by selective laser melting, Compos. Part B Eng. 127 (2017) 26–35. doi:10.1016/j.compositesb.2017.06.026.

[41] P. Guo, B. Zou, C. Huang, H. Gao, Study on microstructure, mechanical properties and machinability of efficiently additive manufactured AISI 316L stainless steel by high-power direct laser deposition, J. Mater. Process. Technol. (2017). doi:10.1016/j.jmatprotec.2016.09.005.

[42] Y. Zhang, L. Yang, J. Dai, Z. Huang, T. Meng, Grain growth of Ni-based superalloy IN718 coating fabricated by pulsed laser deposition, Opt. Laser Technol. (2016). doi:10.1016/j.optlastec.2016.01.015.

[43] V.A. Popovich, E. V. Borisov, A.A. Popovich, V.S. Sufiiarov, D. V. Masaylo, L. Alzina, Functionally graded Inconel 718 processed by additive manufacturing: Crystallographic texture, anisotropy of microstructure and mechanical properties, Mater. Des. (2017). doi:10.1016/j.matdes.2016.10.075.

[44] M. Durand-Charre, The Microstructure of Superalloys, Gordon and Breach Science Publishers, Amsterdam, 1997.

[45] E. Chauvet, P. Kontis, E.A. Jägle, B. Gault, D. Raabe, C. Tassin, J.J. Blandin, R. Dendievel, B. Vayre, S. Abed, G. Martin, Hot cracking mechanism affecting a non-weldable Ni-based superalloy produced by selective electron Beam Melting, Acta Mater. 142 (2018) 82–94. doi:10.1016/j.actamat.2017.09.047.

[46] G. Marchese, E. Bassini, A. Aversa, M. Lombardi, D. Ugues, P. Fino, S. Biamino, Microstructural evolution of post-processed Hastelloy X alloy fabricated by laser powder bed fusion, Materials (Basel). 12 (2019) 486. doi:10.3390/ma12030486.

[47] J. Hicks, Welded joint design - Third edition, Industrial Press Inc., 1999. doi:10.1533/9781855738980.

[48] J.H. Martin, B.D. Yahata, J.M. Hundley, J.A. Mayer, T.A. Schaedler, T.M. Pollock, 3D printing of high-strength aluminium alloys, Nature. 549 (2017) 365–369. doi:10.1038/nature23894.

[49] N.J. Harrison, I. Todd, K. Mumtaz, Reduction of micro-cracking in nickel superalloys processed by Selective Laser Melting: A fundamental alloy design approach, Acta Mater. 94 (2015) 59–68. doi:10.1016/j.actamat.2015.04.035.

[50] P. Kontis, H.A.M. Yusof, S. Pedrazzini, M. Danaie, K.L. Moore, P.A.J. Bagot, M.P. Moody, C.R.M. Grovenor, R.C. Reed, On the effect of boron on grain boundary character in a new polycrystalline superalloy, Acta Mater. (2016). doi:10.1016/j.actamat.2015.10.006.

[51] F. Calignano, Design optimization of supports for overhanging structures in aluminum and titanium alloys by selective laser melting, Mater. Des. 64 (2014) 203–213. doi:10.1016/j.matdes.2014.07.043.

[52] Q. Han, H. Gu, S. Soe, R. Setchi, F. Lacan, J. Hill, Manufacturability of AlSi10Mg overhang structures fabricated by laser powder bed fusion, Mater. Des. 160 (2018) 1080–1095. doi:10.1016/j.matdes.2018.10.043.

[53] I. Maskery, N.T. Aboulkhair, A.O. Aremu, C.J. Tuck, I.A. Ashcroft, Compressive failure modes and energy absorption in additively manufactured double gyroid lattices, Addit. Manuf. 16 (2017) 24–29. doi:10.1016/j.addma.2017.04.003.

[54] S.Y. Choy, C.N. Sun, K.F. Leong, J. Wei, Compressive properties of functionally graded lattice structures manufactured by selective laser melting, Mater. Des. 131 (2017) 112–120. doi:10.1016/j.matdes.2017.06.006.

[55] A.G. Evans, M.Y. He, V.S. Deshpande, J.W. Hutchinson, A.J. Jacobsen, W.B. Carter, Concepts for enhanced energy absorption using hollow micro-lattices, Int. J. Impact Eng. 37 (2010) 947–959. doi:10.1016/j.ijimpeng.2010.03.007.